INTERNATIONAL JOURNAL FOR NUMERICAL METHODS IN FLUIDS
Int. J. Numer. Meth. Fluids 2000; **34**: 711–727

A variationally consistent finite element approach to the two-fluid internal contact-line problem

Nicolas G. Hadjiconstantinou and Anthony T. Patera*,[1]

Department of Mechanical Engineering, Massachusetts Institute of Technology, Cambridge, MA, U.S.A.

SUMMARY

A new method for simulating incompressible viscous fluid flow involving moving internal contact lines is presented. The steady state interface shape is determined by a variationally consistent formulation of the surface tension contribution to the equations of motion adapted to the case of internal contact lines through the application of a global force balance compatibility condition that consistently removes the pressure indeterminacy. The Crouzeix–Raviart element is chosen to capture the pressure discontinuity at the two-fluid interface. The resulting discrete equations are solved by an iterative procedure which displays fast convergence characteristics for small capillary numbers. Numerical results for the case of the steady movement of a fluid meniscus in a two-dimensional channel are presented. Copyright © 2000 John Wiley & Sons, Ltd.

KEY WORDS: internal contact line; global force balance; two-fluid problem

1. INTRODUCTION

The moving contact-line problem remains a challenging problem despite the efforts of many research groups. Although many of the outstanding questions relate to the physical characterization of the problem [1], the numerical solution of the resulting equations also remains a difficult task. On the physical modeling side, researchers are faced with two main challenges: first, the breakdown of the continuum theory at small distances from the contact line manifests itself as a logarithmic stress singularity; and, second, the value of the dynamic contact angle as a function of the interface velocity is undetermined within the continuum framework. Historically, *ad hoc* assumptions that produced agreement with experimental results have been used to achieve closure: slip models can relieve the singularity at the contact point, whereas the assumption that the dynamic contact angle has the same value as the static contact angle appears to be in agreement with experimental results if the slip length is treated as an

* Correspondence to: Department of Mechanical Engineering, Massachusetts Institute of Technology, Room 3-264, 77 Massachusetts Avenue, Cambridge, MA 02139, U.S.A.
[1] E-mail: patera@mit.edu

Received 19 December 1997
Revised 30 January 2000

Copyright © 2000 John Wiley & Sons, Ltd.

adjustable parameter [2]. It has been recognized, however, that the true resolution of the dynamical behavior of contact lines lies in the investigation of the molecular dynamics of contact regions [3,4].

The authors have employed molecular dynamics (MD) simulations [5] of the moving contact-line problem in order to gain further insight into the dynamics of contact-line motion at the molecular scale. These simulations were performed in a two-dimensional channel geometry with two fluids of the same density and viscosity for small capillary numbers $Ca = \mu U/\gamma$, where μ is the fluid viscosity, γ is the surface tension and U is the interface velocity. Continuum simulations in the same geometry were performed and appropriate boundary conditions were found which reproduce the molecularly derived interface shape. It was shown in Reference [5] that, for $Ca \leq 0.072$, the assumption that the dynamic contact angle remains equal to the static contact angle is reasonable, and that slip at the wall is limited to a few (5–10) molecular diameters from the contact line. In this paper, we discuss the continuum technique developed for this investigation. Despite the existence of various techniques, some of which are reviewed below, we feel that no mathematically complete, variationally consistent method, which treats the *internal* moving contact-line problem, has appeared in the literature. This paper describes such a method. We will thus limit ourselves to the mathematical discussion of the moving contact-line problem by using the most common (although *ad hoc*) boundary conditions found in the literature. More information on appropriate boundary conditions is given in Reference [5].

The technique presented in this paper is also used in the validation of a novel hybrid atomistic–continuum simulation technique, where the moving contact-line problem is used as a validation example. In this hybrid approach, the region close to the wall is treated by molecular dynamics, whereas the remainder of the computational domain is treated by the significantly less computationally expensive continuum description. The interested reader is referred to Reference [6].

Although finite element solutions of steady moving contact-line problems first appeared many years ago [2], the complex problem of steady state interface shape determination is not yet entirely resolved. The source of the numerical difficulties is primarily the non-linearity of the problem, which arises (even for Stokes flow) due to the coupling between the two-fluid interface geometry and the two-dimensional flow field.

A common approach to obtaining consistent solutions for both the flow field and the two-fluid interface is to apply a 'segregated' iterative technique: each iteration consists of a flow field solution for a fixed two-fluid interface, followed by a two-fluid interface adjustment. These techniques take advantage of the fact that, in the steady state, the two-fluid interface obeys both (i) the two-fluid stress continuity condition, and (ii) the kinematic condition, which requires the normal fluid velocity at the interface to vanish. A solution can be obtained by relaxing one of these two conditions, and then exploiting the residual of this relaxed condition as the driving force for an improved two-fluid interface geometry.

The exact time-dependent evolution of the two-fluid interface from an arbitrary initial geometry to the steady state is an example of such a procedure. In this case, the kinematic condition is relaxed and the resulting (non-zero) normal velocities on the two-fluid interface then serve to integrate the interface position forward in time. This technique is computationally very inefficient: the time step must be prohibitively small [7,8] due to the very small elements required in the vicinity of the contact line.

Copyright © 2000 John Wiley & Sons, Ltd.

If the dynamics of equilibration are of no interest, and only the steady state solution is required, much faster iterative techniques can be devised [2,7]. In particular, in the work of Lowndes [2], flow field solutions are obtained by relaxing not the kinematic condition, but rather the stress continuity condition. Extension of this work to two-fluid systems is reported in Reference [9]. The Lowndes approach, however, is based upon the strong form of the stress continuity equation, and does not, therefore, constitute a fully consistent finite element treatment of the problem. The latter is not only of interest from a theoretical point of view: variationally consistent schemes are often more accurate and ultimate extension to three space dimensions is arguably simpler.

Consistency is obtained in Ho and Ronquist [7] by application of the appropriate variational form for the traction boundary condition; the latter is first derived in Reference [10] for the two-dimensional case, and subsequently extended in Reference [11] to three dimensions. The residual normal traction supplies the driving force for the motion of the two-fluid interface, just as in Reference [2], but now the variational form of the stress continuity condition is satisfied at equilibrium. The issue of internal contact lines and the resulting pressure indeterminacy is not addressed in Reference [7], however, as the work focuses on free surface flows with no moving contact lines.

The technique presented here may be viewed as a synthesis of the techniques proposed in References [2,7]: the appropriate surface tension variational form and associated normal traction residual is inspired by Reference [7]; the determination of the pressure drop across the interface is addressed through application of a global force balance equation, as first introduced in Reference [2]. In particular, our focus is on the solvability condition that arises as a result of the internal contact line.

2. PHYSICAL PROBLEM

We describe here the physical problem of interest, with particular focus on the conditions associated with the two-fluid interface. The full mathematical description is then given in the next section.

We first consider two static immiscible fluids in a two-dimensional channel: the meniscus that separates the two fluids will adopt a shape that balances the capillary stresses with the pressure difference between the two fluids, subject to the contact angle boundary condition. We next permit the two fluids to move. In particular, we consider the problem in which one fluid displaces the other fluid at a constant interface (average fluid displacement) speed U. The meniscus shape will now further distort due to the stresses created by the flowing fluid; the interface shape is an unknown and must be determined with the flow field by solution of a non-linear set of coupled partial differential equations (PDEs). The problems of interest here are limited to the case of small Reynolds number, $Re \equiv \rho UH/\mu \ll 1$, and small capillary number, $Ca \equiv \mu U/\gamma < 0.1$; here ρ is the density, H is the channel half-width, μ is the dynamic viscosity and γ is the assumed-constant surface tension coefficient between the two fluids.

Finally, we move to the reference frame of the moving interface, as shown in Figure 1. The interface is now stationary and the walls of the channel move in the $\hat{\mathbf{x}}_2$-direction with velocity $-U$. We can further take advantage of the symmetry of the problem and consider only the

Copyright © 2000 John Wiley & Sons, Ltd.

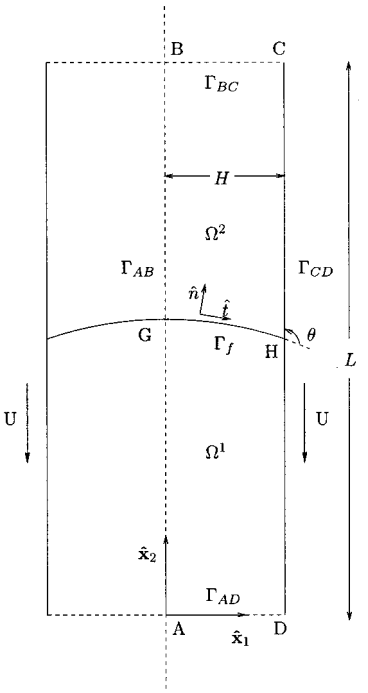

Figure 1. Problem geometry: the domain of interest is $\Omega = \Omega^1 \cup \Omega^2$.

domain Ω, which extends from the wall to the centerline of the channel. Assuming that the channel is sufficiently long [8], the inflow and outflow velocity profiles will be fully developed and hence parabolic. In particular, since in the reference frame of the moving contact line the interface does not move, there can be no fluid displacement; the velocity profiles on Γ_{BC} and Γ_{AD} are thus zero mass flux parabolic profiles that satisfy no-slip ($u_2 = -U$) at the moving wall.

As already indicated, the normal velocity on the two-fluid interface Γ_f must be zero in the steady state. Since the velocity component normal to the wall is necessarily zero, the velocity of the fluid on Γ_f is zero in *both* components at the wall (point H). This, however, is in conflict with the usual no-slip boundary condition at the wall, which would require that fluid particles adjacent to the wall move with velocity $-U$ in the $\hat{\mathbf{x}}_2$-direction. This discrepancy is, of course, the source of the intransigence of the moving contact-line problem. In order to relieve this boundary condition incompatibility, and the resulting shear stress singularity, a slip boundary condition is employed: the fluid velocity at the wall is zero at the contact point (full slip) and smoothly relaxes to $-U$ away from the contact point. The characteristic distance for the decay, l, will be denoted the slip length.

In our simulations we permit slip through two different approaches. In the first approach, we apply the well-known (but admittedly *ad hoc*) Navier condition

Copyright © 2000 John Wiley & Sons, Ltd.

$$\sigma_{21} = -\frac{\mu}{l}(U + u_2) \quad \text{on } \Gamma_{CD} \tag{1}$$

where $u = (u_1, u_2)$ is the fluid velocity and σ_{ij} is the stress tensor. In the second approach, we specify the slip profile, $u_2(x_1 = H, x_2) = \mathscr{U}(x_2)$, as dictated (say) by a MD calculation [5]. In most of this paper we shall focus on the Navier condition; at the conclusion we indicate the necessary changes for the specified velocity approach.

Finally, the contact angle must be specified. The contact angle, θ, is defined as the angle between the bounding wall, Γ_{CD}, and the tangent of Γ_f at the wall, as shown in Figure 1. (The symmetry plane introduces another 'artificial' contact angle (at G) which must be 90°.) Note that the dynamic contact angle θ is not a thermodynamic property, and its specification can, thus, be problematic.

3. VARIATIONAL FORMULATION

We first give the strong form of the equations. The equations governing the fluid flow are the steady incompressible Stokes equations

$$\frac{\partial \sigma_{ij}}{\partial x_j} = 0 \quad \text{in } \Omega \tag{2}$$

$$\frac{\partial u_i}{\partial x_i} = 0 \quad \text{in } \Omega \tag{3}$$

where

$$\sigma_{ij} = \mu\left(\frac{\partial u_i}{\partial x_j} + \frac{\partial u_j}{\partial x_i}\right) - p\delta_{ij} \tag{4}$$

is the stress tensor. Here, p is the pressure and δ_{ij} is the Kronecker delta symbol. We adopt the Einstein summation convention and further assume that all unrepeated indices range from 1 to 2. We neglect gravity forces, although these can, of course, be readily included.

The boundary conditions are then given by

$$\hat{n}_i(\sigma_{ij}|_{\Gamma_f^2} - \sigma_{ij}|_{\Gamma_f^1})\hat{n}_j = \gamma\kappa \quad \text{on } \Gamma_f \tag{5}$$

$$\hat{t}_i(\sigma_{ij}|_{\Gamma_f^2} - \sigma_{ij}|_{\Gamma_f^1})\hat{n}_j = 0 \quad \text{on } \Gamma_f \tag{6}$$

$$\frac{dy_s(0)}{ds} = 0 \tag{7}$$

$$\frac{dy_s(H)}{ds} = \cos\theta \tag{8}$$

Copyright © 2000 John Wiley & Sons, Ltd.

and

$$u_1 = 0 \quad \text{on } \Gamma \tag{9}$$

$$u_2 = Ug \quad \text{on } \Gamma_{AD},\ \Gamma_{BC} \tag{10}$$

and

$$\sigma_{21} = 0 \quad \text{on } \Gamma_{AB} \tag{11}$$

$$\sigma_{21} = -\frac{\mu}{l}(U + u_2) \quad \text{on } \Gamma_{CD} \tag{12}$$

Here $\hat{n}$ and $\hat{t}$ are the right-handed outward unit normal and tangent on Γ_f; Γ_f^2 and Γ_f^1 refer to the limits as we approach Γ_f from Ω^2 and Ω^1 respectively; κ is the curvature; s is the arc length co-ordinate along Γ_f such that $s = 0$ and $s = S$ correspond to points G and H on Γ_f respectively; Γ is the union of Γ_{AB}, Γ_{BC}, Γ_{CD} and Γ_{DA}; $y_s(x_1)$ is the two-fluid interface position as a function of x_1; and g is the parabolic zero mass flux profile, $g(x_1/H) = \frac{1}{2} - \frac{3}{2}(x_1/H)^2$. In what follows, we shall refer only to the non-dimensional form of the governing equations, in which we identify $H = 1$, $U = 1$, $\mu = 1$, $\gamma = Ca^{-1}$ and $l = \varepsilon$.

We now turn to the variational formulation. First, it is convenient to introduce the function spaces $L^2(\Omega)$, $\mathscr{H}^1(\Omega)$, $L_0^2(\Omega)$, $\mathscr{H}_D^1(\Omega)$, $\mathscr{H}_0^1(\Omega)$, $\mathscr{H}_{\Gamma_f}^1(\Omega)$ and $\mathscr{H}_{\Gamma_f 0}^1(\Omega)$. As usual [12], $L^2(\Omega)$ is the space of functions that are square integrable over Ω, and $\mathscr{H}^1$ is the space of functions v such that $v \in L^2(\Omega)$ and $\partial v/\partial x_i \in L^2(\Omega)$. Then

$$L_0^2(\Omega) = \left\{ q \in L^2(\Omega) \middle| \int_{\Omega^1} q \, \mathrm{d}A = 0,\ \int_{\Omega^2} q \, \mathrm{d}A = 0 \right\} \tag{13}$$

$$\mathscr{H}_D^1(\Omega) = \{ v_i \in \mathscr{H}^1(\Omega),\ i = 1, 2 |\ v|_{\Gamma_{AD}} = v|_{\Gamma_{BC}} = (0, g),\ v_1|_{\Gamma_{AB}} = v_1|_{\Gamma_{CD}} = 0 \} \tag{14}$$

$$\mathscr{H}_0^1(\Omega) = \{ v_i \in \mathscr{H}^1(\Omega),\ i = 1, 2 |\ v|_{\Gamma_{AD}} = v|_{\Gamma_{BC}} = 0,\ v_1|_{\Gamma_{AB}} = v_1|_{\Gamma_{CD}} = 0 \} \tag{15}$$

$$\hat{\mathscr{H}}_{\Gamma_f}^1(\Omega) = \{ v_i \in \mathscr{H}^1(\Omega),\ i = 1, 2 |\ v|_{\Gamma_{AD}} = v|_{\Gamma_{BC}} = (0, g),\ v_i \hat{n}_i|_{\Gamma_f} = 0,\ v_1|_{\Gamma_{AB}} = v_1|_{\Gamma_{CD}} = 0 \} \tag{16}$$

$$\hat{\mathscr{H}}_{\Gamma_f 0}^1(\Omega) = \{ v_i \in \mathscr{H}^1(\Omega),\ i = 1, 2 |\ v|_{\Gamma_{AD}} = v|_{\Gamma_{BC}} = 0,\ v_i \hat{n}_i|_{\Gamma_f} = 0,\ v_1|_{\Gamma_{AB}} = v_1|_{\Gamma_{CD}} = 0 \} \tag{17}$$

Note that $\mathscr{H}_D^1$, $\mathscr{H}_0^1$, $\hat{\mathscr{H}}_{\Gamma_f}^1$ and $\hat{\mathscr{H}}_{\Gamma_f 0}^1$ are all product spaces; note also that in $\hat{\mathscr{H}}_{\Gamma_f}^1$ and $\hat{\mathscr{H}}_{\Gamma_f 0}^1$ the tangential component of v is free to vary on Γ_f. Finally, $\mathscr{H}^1(\Gamma_f)$ is the space of scalar functions y for which y and $\mathrm{d}y/\mathrm{d}s$ are square integrable over Γ_f.

We next introduce the bilinear forms

$$a(v, w) = \int_\Omega \frac{\partial v_i}{\partial x_j} \left(\frac{\partial w_i}{\partial x_j} + \frac{\partial w_j}{\partial x_i} \right) \mathrm{d}A + \frac{1}{\varepsilon} \int_{\Gamma_{CD}} v_2 w_2 \, \mathrm{d}s \tag{18}$$

Copyright © 2000 John Wiley & Sons, Ltd.

$$b(v, q) = -\int_{\Omega} \frac{\partial v_i}{\partial x_i} q \, \mathrm{d}A \tag{19}$$

$$b_2(v, q) = -\int_{\Omega^2} \frac{\partial v_i}{\partial x_i} q \, \mathrm{d}A \tag{20}$$

Here, $a(\cdot\,,\cdot)$ is defined and continuous over $\mathscr{H}^1_{\mathrm{D}}$, $\mathscr{H}^1_0$, $\hat{\mathscr{H}}^1_{\Gamma_{\mathrm{f}}}$ and $\hat{\mathscr{H}}^1_{\Gamma_{\mathrm{f}}0}$; similarly, $b(\cdot\,,\cdot)$ is defined and continuous over $X \times L^2(\Omega)$, for $X = \mathscr{H}^1_{\mathrm{D}}$, $\mathscr{H}^1_0$, $\hat{\mathscr{H}}^1_{\Gamma_{\mathrm{f}}}$ and $\hat{\mathscr{H}}^1_{\Gamma_{\mathrm{f}}0}$. Note that $b(v, q) = 0$, $\forall v \in \hat{\mathscr{H}}^1_{\Gamma_{\mathrm{f}}0}$, for q constant in Ω^1 and zero in Ω^2 *and* q constant in Ω^2 and zero in Ω^1; there are two spurious modes when the normal velocity on Γ_{f} is required to vanish.

We shall also need several linear forms. First,

$$\ell^U(v) = -\frac{1}{\varepsilon} \int_{\Gamma_{\mathrm{CD}}} v_2 \, \mathrm{d}s \tag{21}$$

is required for the Navier condition. Second, and more importantly,

$$\ell^\gamma(v;\ y_s) = -Ca^{-1} \int_{\Gamma_{\mathrm{f}}} \frac{\mathrm{d}v_2}{\mathrm{d}s} \frac{\mathrm{d}y_s}{\mathrm{d}s} \, \mathrm{d}s + Ca^{-1} v_2(1) \cos\theta \tag{22}$$

shall represent the surface tension terms. More properly, we should replace the integral in Equation (22) with a duality pairing; also, y may need to be slightly more regular than $\mathscr{H}^1(\Gamma_{\mathrm{f}})$ for the problem to be well posed.

We now look for a velocity u in $\mathscr{H}^1_{\mathrm{D}}(\Omega)$ and a pressure $p = \tilde{p} + \pi$, $\tilde{p}$ in $L^2_0(\Omega)$, π in $\mathbf{R}$, where the latter decomposition permits a pressure level difference between the two fluids. The interface shape y_s is sought in $\mathscr{H}^1(\Gamma_{\mathrm{f}})$. These unknowns must satisfy

$$a(u, v) + b(v, \tilde{p}) + b_2(v, \pi) = \ell^\gamma(v;\ y_s) + \ell^U(v), \quad \forall v \in \mathscr{H}^1_0(\Omega) \tag{23}$$

$$b(u, q) = 0, \quad \forall q \in L^2_0(\Omega) \tag{24}$$

and

$$u_i \hat{n}_i = 0 \quad \text{on } \Gamma_{\mathrm{f}} \tag{25}$$

We can see that Equations (2) and (3) follow from Equations (23) and (24) by taking v to be non-zero in Ω, while Equations (11) and (12) follow by taking v_2 non-zero on Γ_{AB} and Γ_{CD}. The tangential stress continuity equation (6) is enforced by variations in the $\hat{t}$-direction on Γ_{f}; although $u_i \hat{n}_i = 0$ from Equation (25), $v_i \hat{n}_i = 0$ is not constrained in Equation (23), and hence the normal stress continuity equation (5) is also naturally imposed.

Alternatively, we can introduce the following formulation, which makes some of the solvability issues more transparent, and will also be the starting point for the derivation of our two-fluid interface iterative procedure. In this case we look for: $(u, \tilde{p}, \pi, y_s)$ in $(\mathscr{H}^1_{\Gamma_{\mathrm{f}}}(\Omega) \times L^2_0(\Omega) \times \mathbf{R} \times \mathscr{H}^1(\Gamma_{\mathrm{f}}))$ such that

Copyright © 2000 John Wiley & Sons, Ltd.

$$a(u, v) + b(v, \tilde{p}) + b_2(v, \pi) = \ell^U(v), \quad \forall v \in \hat{\mathscr{H}}^1_{\Gamma_f 0}(\Omega) \tag{26}$$

$$b(u, q) = 0, \quad \forall q \in L^2_0(\Omega) \tag{27}$$

and

$$\ell^\gamma(v;\ y_s) = a(u, v) + b(v, \tilde{p}) + b_2(v, \pi) - \ell^U(v), \quad \forall v \in \mathscr{H}^1_0(\Omega) \tag{28}$$

In this formulation, $u_i \hat{n}_i = 0$ of Equation (25) is actually imposed by the appropriate choice of space, $\hat{\mathscr{H}}^1_{\Gamma_f}(\Omega)$. However, since $v_i \hat{n}_i = 0$ for v in $\hat{\mathscr{H}}^1_{\Gamma_f 0}(\Omega)$, Equation (26) only imposes the tangential stress condition, not the normal stress continuity equation (5); the latter condition is now enforced by Equation (28).

Equations (22) and (23) involve the x_2 component of the normal stress continuity equation (5). It can be shown that if this condition is satisfied, then the complete variational-weak formulation of Equation (5) is also satisfied

$$a(u, v) + b(v, \tilde{p}) + b_2(v, \pi) - \ell^U(v) = \Lambda^\gamma(v;\ x_s), \quad \forall v \in \mathscr{H}^1_0(\Omega) \tag{29}$$

where

$$\Lambda^\gamma(v;\ x_s) = -Ca^{-1} \int_{\Gamma_f} \frac{\mathrm{d}v_i}{\mathrm{d}s} \frac{\mathrm{d}x_{si}}{\mathrm{d}s}\, \mathrm{d}s + Ca^{-1} v_2(1) \cos\theta \tag{30}$$

and $x_s = (x_{s1}, x_{s2}) = (x_{s1}, y_s)$ are the co-ordinates of the two-fluid interface Γ_f [10]. To show this, we first note that we can express any v as $v_1 \hat{\mathbf{x}}_1 + v_2 \hat{\mathbf{x}}_2$, and that, thanks to Equation (28), the $v_2 \hat{\mathbf{x}}_2$ contribution to Equation (29) clearly vanishes. We next note that if $\hat{t}_1$ is always non-zero, then $v_1 \hat{\mathbf{x}}_1$ may be expressed as $\Psi + \Phi$, where $\Psi|_{\Gamma_f} = v_1 \hat{t}/\hat{t}_1$ and $\Phi|_{\Gamma_f} = -v_1 \hat{t}_2/\hat{t}_1 \hat{\mathbf{x}}_2$. These contributions to Equation (29) also vanish—the former due to Equation (26) and the latter due to Equation (28)—and the result is thus proven. Cases in which $\hat{t}_1$ may vanish, for example, fully wetting configurations, are beyond the scope of the current investigation.

We know, on physical grounds, that the pressure level is indeterminate. However, as already discussed, $b(v, q)$ has *two* spurious modes for $u \in \hat{\mathscr{H}}^1_{\Gamma_f 0}(\Omega)$, and hence to render $\tilde{p}$ unique in Equation (26) $L^2_0(\Omega)$ requires zero average in both domains, which is clearly overconstrained. To rectify the situation we have introduced the scalar π, which must be determined by a global force balance. In fact, this global force balance represents the (left null space) solvability condition associated with the indeterminacy (right null space) of the (say) average position of the free surface.

In particular, it is clear from Equations (22) and (28) that the solution is translationally invariant: we may add any constant to y_s with impunity. From the 'left' side we notice that the surface Laplacian is annihilated by any function in $\mathscr{H}^1_0(\Omega)$, such that $v_2 = 1$ on Γ_f. The associated solvability condition—our equation for π— is given by

$$Ca^{-1} \cos\theta = \{a(u, v) + b(v, \tilde{p}) + b_2(v, \pi) - \ell^U(v)\}, \quad \forall v \in \{\mathscr{H}^1_0(\Omega) |\ v_2|_{\Gamma_f} = 1\} \tag{31}$$

Copyright © 2000 John Wiley & Sons, Ltd.

which is just the variational form of the normal force balance on Γ_f

$$Ca^{-1}\cos\theta = \int_0^S (\sigma_{2j}|_{\Gamma_f^2} - \sigma_{2j}|_{\Gamma_f^1})\hat{n}_j \, \mathrm{d}s = \int_0^1 \hat{n}_i(\sigma_{ij}|_{\Gamma_f^2} - \sigma_{ij}|_{\Gamma_f^1})\hat{n}_j \, \mathrm{d}x_1 \tag{32}$$

as derived in Reference [1]. Recall that θ is the imposed dynamic contact angle. Note that, because u is in equilibrium from Equation (26), π is insensitive to the particular lifting of v chosen in Equation (31); numerical convenience will suggest an obvious candidate, as we discuss in Section 5.

4. DISCRETE EQUATIONS

We first introduce the finite element approximation (u_{hi}, p_h) to (u_i, p) over a suitable triangulation $\mathscr{T}_h$ of Ω such that

$$\bar{\Omega} = \bigcup_k \bar{T}_h^k$$

where T_h^k are the triangular elements. The variable geometry requirements necessitates the application of an isoparametric formulation in which the mid-points of the sides of elements for which the end-points lie on Γ are displaced so as to also lie on Γ. The resulting isoparametric mapping F^k from the reference element $\hat{T}$ to T_h^k, depicted in Figure 2, takes the form

$$(x_1(\boldsymbol{\xi}), x_2(\boldsymbol{\xi})) = \sum_{i=1}^{6} (x_1, x_2)_i h_i(\boldsymbol{\xi}) \tag{33}$$

where the h_i are the usual quadratic reference element shape functions, $(x_1, x_2)_i$ are the co-ordinates of the six elemental boundary nodes, and $\boldsymbol{\xi}$ is the vector of reference element

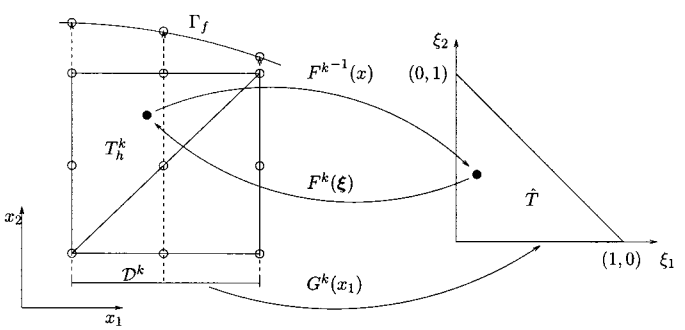

Figure 2. Elemental mappings.

Copyright © 2000 John Wiley & Sons, Ltd.

(barycentric) co-ordinates $(\xi_1, \xi_2, 1-\xi_1-\xi_2)$. The Jacobian of the transformation is a quadratic function of $\boldsymbol{\xi}$.

In order to simplify our task, we shall require that nodes on Γ_f are equispaced in the $\hat{\mathbf{x}}_1$-direction, and that the x_1 location of these nodes is fixed during the iterative process to be discussed in Section 5. This implies that x_1 on Γ_f in element T_h^k is a linear function of (say) ξ_1, $F_{x_1}^k(\xi_1)$, and hence the inverse edge mapping $\xi_1 = G^k(x_1)$ exists and is also linear. We deduce that

$$y_s = F_{x_2}^k(\xi_1) = F_{x_2}^k \circ G^k(x_1) \tag{34}$$

is piecewise quadratic in x_1 and thus $y_s \in Y_s \equiv \{y|_{\mathscr{D}_k} \in \mathbf{P}_2(\mathscr{D}^k),\ \forall \mathscr{D}^k \in \Gamma_{\mathscr{D}}\} \cap \mathscr{H}^1(\Gamma_f)$, where $\mathscr{D}^k$ is the projection of T_h^k onto the x_1 axis, $\mathbf{P}_q(\mathscr{D}^k)$ is the space of the qth-order polynomials over $\mathscr{D}^k$, and $\bar{\Gamma}_{\mathscr{D}} = \cup_k \bar{\mathscr{D}}^k$.

The complete statement of the discrete problem is then: find $(u_h, \tilde{p}_h, \pi_h, y_{sh}) \in (X_h, Y_h, \mathbf{R}, Y_s)$ such that

$$a_h(u_h, v) + b_h(v, \tilde{p}_h) + b_{2h}(v, \pi_h) = \ell^U(v), \quad \forall v \in W_{h\Gamma_f 0}(\Omega) \tag{35}$$

$$b_h(u_h, q) = 0, \quad \forall q \in Y_h \tag{36}$$

and

$$\ell^\gamma(v;\ y_{sh}) = a_h(u_h, v) + b_h(v, \tilde{p}_h) + b_{2h}(v, \pi_h) - \ell^U(v), \quad \forall v \in W_{h0} \tag{37}$$

where

$$X_h = \{v|_{T_h} = v \circ F^{k^{-1}},\ v \in \mathbf{P}_2^+(\hat{T}),\ \forall T_h \in \mathscr{T}_h\} \cap \mathscr{H}^1_{\Gamma_f}(\Omega) \tag{38}$$

$$Y_h = \{q|_{T_h} = q \circ F^{k^{-1}},\ q \in \mathbf{P}_1(\hat{T}),\ \forall T_h \in \mathscr{T}_h\} \cap L^2_0(\Omega) \tag{39}$$

$$W_{h\Gamma_f 0} = \{v|_{T_h} = v \circ F^{k^{-1}},\ v \in \mathbf{P}_2^+(\hat{T}),\ \forall T_h \in \mathscr{T}_h\} \cap \mathscr{H}^1_{\Gamma_f 0}(\Omega) \tag{40}$$

$$W_{h0} = \{v|_{T_h} = v \circ F^{k^{-1}},\ v \in \mathbf{P}_2^+(\hat{T}),\ \forall T_h \in \mathscr{T}_h\} \cap \mathscr{H}^1_0(\Omega) \tag{41}$$

and

$$\mathbf{P}_2^+(\hat{T}) = \{\mathbf{P}_2(\hat{T}) + \alpha_{T_h} \xi_1 \xi_2 \xi_3,\ \alpha_{T_h} \in \mathbf{R}\} \tag{42}$$

is the space of quadratic polynomials enhanced by a cubic bubble function. (Note that the π_h term in Equation (35) does not in fact contribute.)

This particular choice of the Crouzeix–Raviart element is very well suited for two-fluid interface problems: pressure continuity is not enforced across elemental boundaries, thus enabling the solution to correctly capture the surface tension-induced pressure discontinuity across the two-fluid interface. (We recall the cubic bubble function is added to sufficiently

Copyright © 2000 John Wiley & Sons, Ltd.

enrich the velocity degrees of freedom so that these elements, which have substantially more pressure degrees of freedom than the continuous pressure Taylor–Hood elements, still satisfy the *inf–sup* condition.) The subscript h on the linear and bilinear forms indicates the approximation introduced by the isoparametric representation of the problem geometry, and the resulting application of quadrature rules [13] for the evaluation of the elemental integrals. In this work, a seven-point quadrature rule is used.

5. ITERATIVE INTERFACE PROCEDURE

Equation (37) is the point of departure for the derivation of the variational form for the iterative interface procedure. We exploit the fact that the two sides of Equation (37) will not balance unless the steady state solution has been achieved; we can thus use the residual of (37) as a force to drive the interface shape towards the steady state solution. More specifically, we write $y_s = y_s + \Delta y$, and thereby obtain a Laplacian operator for the 'correction' displacement Δy

$$-\int_0^S \frac{\partial v_2}{\partial s}\frac{\partial \Delta y_{sh}}{\partial s}\,\mathrm{d}s = \int_0^S \frac{\partial v_2}{\partial s}\frac{\partial y_{sh}}{\partial s}\,\mathrm{d}s - v_2(1)\cos\theta - Ca(a_h(u_h, v) + b_h(v, \tilde{p}_h) + b_{2h}(v, \pi_h) - \ell^U(v)), \quad \forall v \in W_{h0}(\Omega) \tag{43}$$

When the iteration has converged, $\Delta y = 0$, and the above equation reduces to Equation (37), which must be satisfied in the steady state.

Note that although two Neumann boundary conditions—two angles, one the contact angle and the other the symmetry condition—can be specified for this problem, this would result in an ill-posed problem, since the absolute level of y_s would be allowed to 'float'; this reflects the invariance of Equation (37) under an arbitrary displacement in the $\hat{\mathbf{x}}_2$-direction as discussed in Section 3. To ensure uniqueness, only the symmetry Neumann condition is used along with a *Dirichlet* boundary condition of zero displacement at some other location (in particular, the wall), which thus specifies the two-fluid interface displacement level. Solvability is ensured by the correct choice of π as per Equation (31).

The complete solution algorithm then consists of the following steps:

1. Solve the discrete Stokes equations (35) and (36) for u_h, $\tilde{p}_h$ for some given initial geometry y_s^0.
2. Solve

$$b_{2h}(v, \pi_h) = Ca^{-1}\cos\theta - \{a_h(u_h, v) + b_h(v, \tilde{p}_h) - \ell^U(v)\} \tag{44}$$

to find π_h. The numerical value of $\{a_h(u_h, v) + b_h(v, \tilde{p}_h)\}$ is simply the sum of the stress 'residuals' on Γ_f, i.e., the sum of the entries corresponding to the $\hat{\mathbf{x}}_2$-direction velocity nodes lying on Γ_f of the vector that results from multiplying the stiffness matrix with the solution obtained in step (1). The set of coefficients $b_{2h}(v, \pi_h)$ can be easily obtained by multiplying the stiffness matrix by a vector whose non-zero entries are unity at all pressure nodes on

Copyright © 2000 John Wiley & Sons, Ltd.

one side of Γ_f. Note that these evaluations correspond to the choice $v \in \{W_{h0}(\Omega) |\ v_2|_{\Gamma_f} = 1\}$ in which $v_1 = 0$ and v_2 is the sum of all the nodal basis functions associated with Γ_f.

3. Apply

$$-\int_0^S \frac{\partial v_2}{\partial s}\frac{\partial \Delta y_{sh}}{\partial s}\,\mathrm{d}s = \int_0^S \frac{\partial v_2}{\partial s}\frac{\partial y_{sh}}{\partial s}\,\mathrm{d}s - v_2(1)\cos\theta - Ca(a_h(u_h, v) + b_h(v, \tilde{p}_h) + b_{2h}(v, \pi_h) - \ell^U(v)), \quad \forall v \in W_{h0}(\Omega) \tag{45}$$

to calculate the 'corrected' interface shape.

4. Repeat the procedure to convergence.

For low *Ca* the method converges quite rapidly, as we discuss below.

6. NUMERICAL RESULTS

6.1. Triangulations

We next describe the meshes that we shall use in the examples, although our scheme is in no way limited to any particular triangulation strategy. For simplicity, we shall consider structured meshes, in particular structured meshes in which the degrees of freedom are concentrated near the contact line. These resulting meshes do not satisfy the shape regularity condition as $h \to 0$ [14]; however, for the h studied here we do not believe that the error is adversely affected by this transgression. In particular, we obtain similar results for (much more expensive) uniform and regular structured meshes. Future work will also consider unstructured meshes, which are clearly the best choice, and will permit us to perform more conclusive spatial convergence studies; our focus here, however, is on the finite element formulation.

It has been suggested [1] that, for the complete resolution of the slip phenomenon, the element size close to the contact line must be much smaller than l, the slip length, due to the weak (logarithmic) singularity in the velocity gradient and pressure as the contact line is approached. We satisfy this requirement with a mesh that is fairly coarse away from the interface and wall, but rather fine in the vicinity of Γ_f and Γ_{CD}. More specifically, we begin with a 'background' grid of 5×10 element pairs in the $\hat{\mathbf{x}}_1$- and $\hat{\mathbf{x}}_2$-directions respectively. Further refinement in the $\hat{\mathbf{x}}_1$-direction is subsequently achieved by splitting the last element (close to the wall) in a 3:1 ratio. The refinement in the $\hat{\mathbf{x}}_2$-direction is obtained by applying an analogous procedure to the layer of two elements enclosing the two-fluid interface. For example, a 8×18 mesh specification implies that the element closest to the wall in the $\hat{\mathbf{x}}_1$-direction has been successively divided in a 3:1 ratio three times, yielding a smallest element (the elements closest to the wall) with an edge size of $0.2 \cdot (0.25)^3 = 3.125\mathrm{e}-3$; similarly, the smallest element edge size in the $\hat{\mathbf{x}}_2$-direction (the elements closest to Γ_f) is $0.5 \cdot 0.2 \cdot (0.25)^4 = 3.906\mathrm{e}-4$.

Figure 3 demonstrates the 'background' grid and the first level of refinement, a 6×12 grid; in the case illustrated in Figure 3, Γ_f is flat. When Γ_f is curved, a linear stretching in $\hat{\mathbf{x}}_2$ is

Copyright © 2000 John Wiley & Sons, Ltd.

applied as a function of the element distance from Γ_f, with the dilation reducing to zero on Γ_{AD} and Γ_{BC}; this ensures compatibility between the problem geometry and the finite element mesh. The advantage of this mesh is that very fine elements are produced near the contact line H, with a relatively small total number of elements. The main disadvantage, as already indicated, is that the angles in elements close to G, C and D are not bounded away from zero as we increase the number of elements indefinitely [14].

6.2. Numerical examples

The length of the channel is chosen to extend three channel half-widths in each direction ($L = 6$) so that the assumption of fully developed flow at inflow and outflow is justified [8]. In all cases presented here we set $\varepsilon = 0.01$, $\theta = 100°$ and consider a 10×24 mesh; only Ca is varied. Figures 4 and 5 show the converged solution for $Ca = 0.02$. To the authors' knowledge, this is the first study of the dynamics of contact-line motion in a two-dimensional channel, and thus no numerical or experimental results are available for direct comparison. Our results for interface shapes as a function of Ca are, however, in qualitative agreement with the axisymmetric results of Reference [15], which considers the contact line involving two fluids of the same viscosity in a tube.

The existence of secondary recirculation regions in the advancing fluid (here Ω^1) is reported in References [9,15]. Mavrides *et al.* [9], using a velocity profile along the slip wall rather than a Navier condition, found that the recirculation region occurs in the less viscous fluid. Similar results for fluids of the same viscosity are presented in Reference [15]. We confirm the existence of secondary recirculation regions close to points G and H, in qualitative agreement with the results of Reference [15] for the same choice of parameters ($Ca = 0.001$, $\theta = 40°$, $\varepsilon = 0.006$). (Note, however, that our slip model and that of Reference [15] are not the same.)

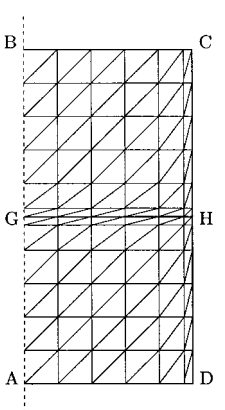

Figure 3. A 6×12 finite element grid.

Copyright © 2000 John Wiley & Sons, Ltd.

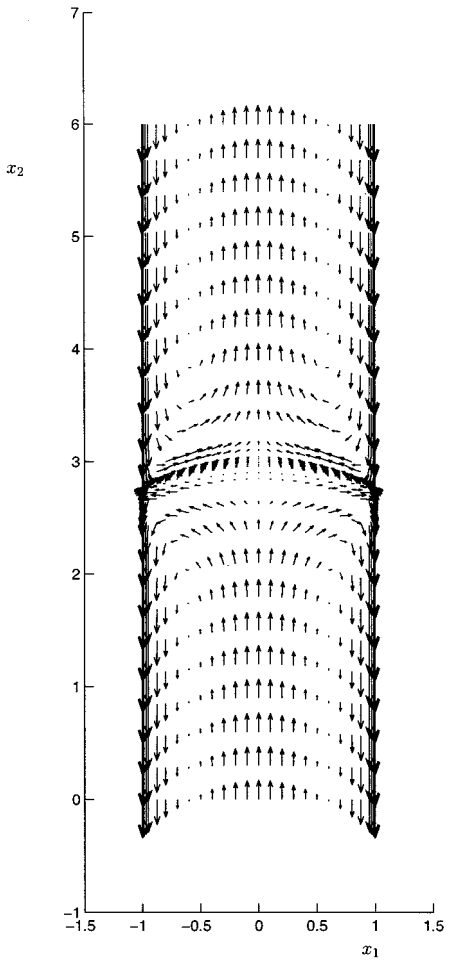

Figure 4. Velocity solution for $Ca = 0.02$.

The iterative procedure exhibits fast convergence characteristics. Figure 6 shows the intermediate two-fluid interface geometries obtained en route to convergence starting from a horizontal flat interface. In this example ($Ca = 0.02$) the maximum Δy change is less than 10^{-4} after four iterations. Note that the convergence is slower as Ca increases, since the importance of capillary forces diminishes [7]. The convergence rate is also sensitive to the slip length: for $\varepsilon \sim O(10^{-2})$ underelaxation—only a fraction (typically not smaller than 1/5) of the computed 'correction displacement' Δy is used to obtain the next interface geometry—is required for $Ca > 0.05$, whereas for $\varepsilon \sim O(1)$ underelaxation is required only for $Ca > 0.1$. Figure 7 shows the convergence process for π as a function of the iteration number for $Ca = 0.02$. We notice that π takes somewhat longer to fully converge than the two-fluid interface shape, which is a manifestation of the fact that it is fairly sensitive to small changes to the shape of Γ_f.

Copyright © 2000 John Wiley & Sons, Ltd.

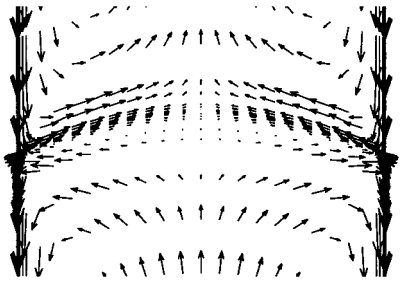

Figure 5. Velocity solution close to the interface for $Ca = 0.02$.

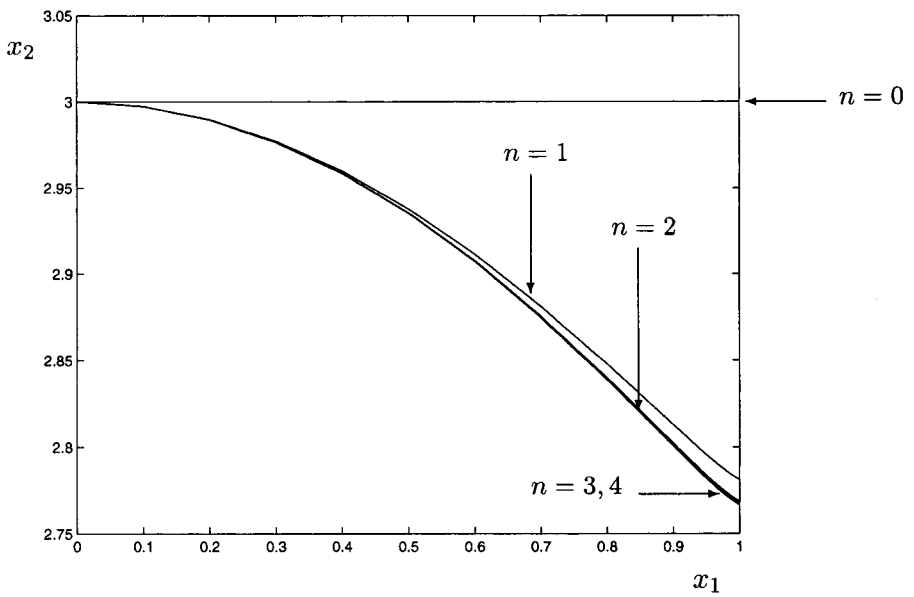

Figure 6. Two-fluid interface geometry convergence history for $Ca = 0.02$ ($n =$ iteration number). Note that the axes are not drawn to scale to emphasize the differences between the various iterates.

Christodoulou and Scriven [16] report that the imposition of the dynamic contact angle as a weak boundary condition resulted in large deviations between the desired and the observed dynamic contact angle. This problem may be related to their iterative solution technique, which additionally did not converge for a wide range of dynamic contact angles. For this reason they resorted to imposing the dynamic contact angle as an essential boundary condition. We did not face any of the above problems although our capillary numbers were restricted to $Ca < 0.1$ and the slip length was only a few orders of magnitude smaller than the computational domain ($\varepsilon > 10^{-3}$).

Copyright © 2000 John Wiley & Sons, Ltd.

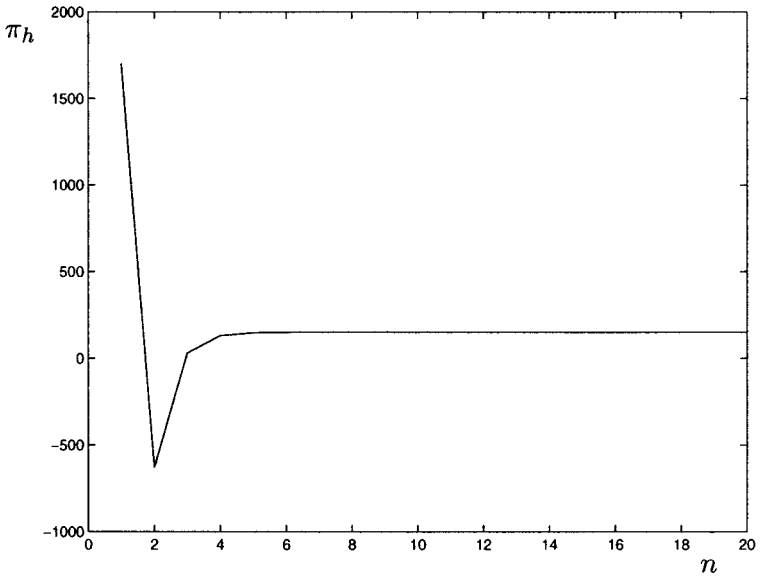

Figure 7. π_h convergence history for $Ca = 0.02$ (n = iteration number).

Our spatial convergence studies include the comparison of interface shapes for $Ca = 0.02$ as a function of the mesh size. Various mesh resolutions are used between 8×20 (the coarsest) and 12×28 (the finest). The two-fluid interface shapes obtained with the two most refined meshes (11×26 and 12×28) exhibit a maximum Δy deviation of less than 10^{-4}, suggesting that spatial convergence has, indeed, been obtained. The sensitivity of π to the exact shape of Γ_f is again obvious in these tests: π still changes by 0.3 per cent in proceeding from a mesh of 11×26 to a mesh of 12×28.

We also investigated the case of a specified slip profile along Γ_{CD}, $u_2(x_1 = H, x_2) = \mathscr{U}(x_2)$. The only change necessary to the formulation presented in this paper is the replacement of the natural boundary condition along Γ_{CD} with an essential boundary condition. We remark that the velocity degrees of freedom on the slipping wall are now excluded from the solution space of Equation (35), and thus π (Equation (44)) is 'contaminated' by the residual of the equations involving those degrees of freedom. To illustrate this further, if we take v in Equation (44) to be $v_1 = 0$ in Ω_h (the discretized domain) and $v_2|_{\Gamma_f} = 1$ and $v_2 = 0$ on all nodes not lying on Γ_f, we see that there exists an additional contribution from the part of v_2 untested in Equation (35). This single-element contribution, however, is expected to vanish as $h \to 0$, and thus should not influence the results of our simulation when h is small.

We have verified the above assertion using the following method. We first compute the slip profile along Γ_{CD} for the baseline example presented above using the Navier slip condition with $\varepsilon = 0.01$, $Ca = 0.02$, a 10×24 mesh and a convergence criterion that the maximum Δy is less than 10^{-6}. We then use this slip profile as a Dirichlet boundary condition in a new

Copyright © 2000 John Wiley & Sons, Ltd.

specified slip simulation with a similarly tight convergence criterion. We find that the difference between the converged interface shapes predicted by the two simulations is less than 10^{-6}.

7. CONCLUSIONS

We have developed a new variationally consistent numerical solution technique for problems involving internal contact lines. The pressure indeterminacy is successfully removed by a force balance compatibility condition. The associated interface iterative method displays fast convergence characteristics for $Ca < 0.1$.

ACKNOWLEDGMENTS

This work was supported by DARPA and the ONR under Grant N00014-91-J-1889.

REFERENCES

1. Dussan EB. On the spreading of liquids on solid surfaces: static and dynamic contact angles. *Annual Review of Fluid Mechanics* 1979; **11**: 371–400.
2. Lowndes J. The numerical simulation of the steady movement of a fluid meniscus in a capillary tube. *Journal of Fluid Mechanics* 1980; **101**: 631–646.
3. Blake TD, Haynes JM. Kinetics of liquid/liquid displacement. *Journal of Colloid and Interface Science* 1969; **30**: 421–423.
4. Thompson PA, Robbins MO. Simulations of contact-line motion: slip and the dynamic contact angle. *Physical Review Letters* 1989; **63**: 766–769.
5. Hadjiconstantinou NG. Combining atomistic and continuum simulations of contact-line motion. *Physical Review E* 1999; **59**: 2475–2478.
6. Hadjiconstantinou NG. Hybrid atomistic–continuum formulations and the moving contact-line problem. *Journal of Computational Physics* 1999; **154**: 245–265.
7. Ho L, Ronquist EM. Spectral element solution of steady incompressible viscous free-surface flows. *Finite Elements in Analysis and Design* 1994; **16**: 207–227.
8. Bazhlekov IB, Chesters AK. Numerical investigation of the dynamic influence of the contact line region on the macroscopic meniscus shape. *Journal of Fluid Mechanics* 1996; **329**: 137–146.
9. Mavridis H, Hrymak AN, Vlachopoulos J. Finite element simulation of stratified multiphase flows. *AIChE Journal* 1987; **33**(3): 410–422.
10. Ruschak KJ. A method for incorporating free boundaries with surface tension in finite element fluid-flow simulation. *International Journal for Numerical Methods in Fluids* 1980; **15**: 639–648.
11. Ho LW, Patera AT. Variational formulation of three-dimensional viscous free-surface flows: natural imposition of surface tension boundary conditions. *International Journal for Numerical Methods in Engineering* 1991; **13**: 691–698.
12. Adams RA. *Sobolev Spaces*. Academic Press: New York, 1975.
13. Kikuchi N. *Finite Element Methods in Mechanics*. Cambridge University Press: Cambridge, 1986.
14. Quarteroni A, Valli A. *Numerical Approximation of Partial Differential Equations*. Springer: Berlin, 1994.
15. Sheng P, Zhou M. Immiscible-fluid displacement: contact-line dynamics and the velocity-dependent capillary pressure. *Physical Review A* 1992; **45**: 5694–5708.
16. Christodoulou KN, Scriven LE. The fluid mechanics of slide coating. *Journal of Fluid Mechanics* 1989; **208**: 321–354.

Copyright © 2000 John Wiley & Sons, Ltd.